Supporting Information

Experimental and theoretical comparison of potential-dependent methylation on chemically exfoliated WS_2 and MoS_2

Ellen X. Yan,[†] Renata Balgley,[†] Maureen B. Morla,[†] Soonho Kwon,[§] Charles B. Musgrave,[§] Bruce S. Brunschwig,[‡] William A. Goddard III,[§] and Nathan S. Lewis[*,†,‡]

[†]Division of Chemistry and Chemical Engineering, [‡]Beckman Institute, [§]Material and Process Simulation Center, California Institute of Technology, Pasadena, California 91125, United States

*nslewis@caltech.edu

Table of Contents

I. Analyses and Calculations

1. Analysis and quantification of coverage from XPS data

High-resolution XPS data were analyzed using CasaXPS software v. 2.3.17. A Shirley background was applied to all C 1*s*, S 2*p*, Mo 3*d*, and W 4*f* spectra, with endpoints averaged from 21 points. Spectra were calibrated by setting the C1*s* peak at 284.8 eV. Peaks were fitted according to the constraints listed below, and the coverage per sulfur atom was obtained using the area of the functionalized sulfur peaks divided by the total area of all sulfur peaks. This value was doubled to obtain the coverage per MS_2 unit (M = Mo, W). Although a similar value can be obtained by quantifying the sulfur peaks relative to the transition metal peaks, a comparison within the same XPS binding energy region removes errors associated with any changes in the inelastic mean free path (IMFP) of photoelectrons as the kinetic energy is changed.

Lineshapes

The W 4*f* and Mo 3*d* peaks were fit using a modified Lorentzian asymmetric lineshape with tail damping, LF(α, β, *w*, *m*), where α and β determine the tail asymmetry, *w* is the tail damping parameter, and *m* defines the width of the Gaussian. LF(1,1,55,260) was used to fit all Mo 3*d* peaks based on previous reports modelling Mo XPS peaks[1] and LF(1.6,1.6,75,260) was used to fit all W 4*f* and W 5*p*3/2 peaks in order to minimize the residual standard deviation (residual STD) by adjusting the tail. Mo 3*d* and W 4*f* peaks are symmetrical except in the case of pure Mo and W metal.[2] The S 2*s* peak in the Mo 3*d* region was fit using a Lorentzian asymmetric lineshape, LA(α, β, *m*), with parameters LA(2,2,50) by matching the experimental data and minimizing the residual STD between the fit and the data in CasaXPS. S 2*p* peaks were fit using a Voigt GL(30) function with 70% Gaussian and 30% Lorentzian character, which resulted in a minimum in the residual STD.

Constraints

Due to spin-orbit coupling, the Mo 3*d*, W 4*f*, and S 2*p* peaks are doublets with specific area ratios and position constraints. The following constraints were placed:

- area(Mo $3d_{3/2}$) = area(Mo $3d_{5/2}$) × 0.67
- FWHM(Mo $3d_{3/2}$) = FWHM(Mo $3d_{5/2}$) ± 0.2
- position(Mo $3d_{3/2}$) = position(Mo $3d_{5/2}$) + 3.13 eV
- area(W $4f_{5/2}$) = area(W $4f_{7/2}$) × 0.75
- FWHM(W $4f_{5/2}$) = FWHM(W $4f_{7/2}$)
- position(W $4f_{5/2}$) = position(W $4f_{7/2}$) + 2.17 eV
- area(S $2p_{1/2}$) = area(S $2p_{3/2}$) × 0.5
- FWHM(S $2p_{1/2}$) = FWHM(S $2p_{3/2}$)
- position(S $2p_{1/2}$) = position(S $2p_{3/2}$) + 1.18 eV

In addition, the ratios of the areas and positions of the 2H to 1T′ S 2*p* peaks were determined from the average of the unconstrained fitting of *ce*MoS_2 and *ce*WS_2 samples (2 each) that were handled completely under inert atmosphere including air-free transfer to the XPS instrument. These ratios were used to constrain the ratios of 2H to 1T′ S 2*p* in the analysis of functionalized samples to

avoid over- or under-fitting the functionalized sulfur peak. The following constraints were applied to fct-MoS_2 and fct-WS_2 spectra:

- area(MoS_2(2H) S 2*p*) = area(MoS_2(total) S 2*p*) × 0.18
- area(MoS_2(2H) Mo 3*d*) = area(MoS_2(total) Mo 3*d*) × 0.18
- position(MoS_2(2H) S $2p_{3/2}$) = position(MoS_2(1T′) S $2p_{3/2}$) + 1.0 eV
- position(MoS_2(S*) S $2p_{3/2}$) = position(MoS_2(1T′) S $2p_{3/2}$) – 0.61 eV

- area(WS_2(2H) S 2*p*) = area(WS_2(total) S 2*p*) × 0.18
- area(WS_2(2H) W 4*f*) = area(WS2(total) W 4*f*) × 0.18
- position(WS_2(2H) S $2p_{3/2}$) = position(WS_2(1T′) S $2p_{3/2}$) + 1.12 eV
- position(WS_2(S*) S $2p_{3/2}$) = position(WS_2(1T′) S $2p_{3/2}$) – 0.61 eV

Note that since the values above were determined from 2 samples, additional samples will improve the accuracy of the estimate for these constraints and would change the quantification values for individual samples accordingly. Even so, a given set of constraints produces a reliable method of fitting and comparison between samples, thus we proceeded with the above constraints with the disclaimer that should different constraints be applied, the fittings would change accordingly. For instance, increasing the distance between 2H and 1T S $2p_{3/2}$ peaks from 1.12 to 1.17 eV, keeping all other parameters constant, results in an decrease of 0.7% in the calculated coverage per WS_2, which is negligible considering the variability between samples of 2-5% in most conditions. To provide a metric of variability, below are the average ± standard deviation of fitting parameters found from fitting *ce*MoS_2 and *ce*WS_2 samples that were used to inform the above constraints:

- area(MoS_2(2H) S 2*p*) / area(MoS_2(total) S 2*p*) = 0.18 ± 0.02
- position(MoS_2(2H) S $2p_{3/2}$) – position(MoS_2(1T′) S $2p_{3/2}$) = 0.979 ± 0.003 eV
- position(MoS_2(S*) S $2p_{3/2}$) – position(MoS_2(1T′) S $2p_{3/2}$) = –0.62 ± 0.006 eV

- area(WS_2(2H) S 2*p*) / area(WS_2(total) S 2*p*) = 0.18 ± 0.018
- position(WS_2(2H) S $2p_{3/2}$) – position(WS_2(1T′) S $2p_{3/2}$) = 1.12 ± 0.13 eV
- position(WS_2(S*) S $2p_{3/2}$) – position(WS_2(1T′) S $2p_{3/2}$) = –0.60 ± 0.04 eV

2. Work functions of *ce*MoS_2 and *ce*WS_2

The high-binding energy region of the UPS spectra for *ce*MoS_2 and *ce*WS_2 (2 each) shown in Figure S3 were fitted using linear regression to determine the point at which the linear fit intersects the x-axis. This cutoff value was then used to calculate the work function using the formula WF = *E*(He I) – BE(cutoff) = 21.22 eV – BE(cutoff). Samples were handled under inert conditions using air-free transfer to obtain the UPS spectra.

3. Effective reduction potential for one-electron reductants

The standard potential for the one-electron redox couple corresponding to each of the reductants used in our experiments was obtained from literature using values obtained in acetonitrile but shifted by +30 mV based on the difference in formal potentials for the ferrocenium/ferrocene redox

couple in acetonitrile vs DMF.[3-4] This conversion affects only the comparison between the MoS_2 and WS_2 work functions and the reductant on the absolute energy scale, for which we used E_{vac} = –4.44 V vs SHE, $E(Fc^{+/0})$ = 0.544 V vs Ag/AgCl/KCl(sat'd),[4] and E(Ag/AgCl/KCl(sat'd)) = 0.20 V vs SHE, resulting in an overall of $E(Fc^{+/0})$ = 5.18 V vs E_{vac}. The effective reduction potential for a solution where only the reductant was added was estimated from the Nernst equation assuming a 50:1 ratio of reductant to oxidant (i.e. 98% purity), resulting in a correction of –0.1 V to obtain the effective potentials in Figure 2 and Table S1.

$$E_{\text{eff}} = E(\text{A}/\text{A}^-) - \frac{RT}{zF}\ln\frac{a_{\text{Red}}}{a_{\text{Ox}}}$$

4. Grand Canonical Potential Density Functional Theory

We used the Grand Canonical Potential Kinetics (GCP-K) method[57] to predict the reaction free energy changes and activation free energies from Quantum Mechanics (QM) as a function of applied potential. This allows comparisons directly with experimental data. The QM calculations are carried out as a function of the number of electrons. Then we use the Legendre transform in Eqn. (1)to transform to applied potenial, U. [5]

$$G(n; U) = F(n) - ne(U_{\text{SHE}} - U) \quad (1)$$

We require that

$$\frac{\text{dG(n;U)}}{\text{dn}} = 0 \; or \; \mu_e = e(U_{SHE} - U) = \frac{\text{dF(n)}}{\text{dn}} \quad (2)$$

this determines the optimum number of electrons for each U.

$F(n)$ depends quadratically on the number of electrons, leading to

$$F(n) = a(n - n_0)^2 + b(n - n_0) + c \quad (3)$$

where n_0 is the number of electrons in a neutral system

This leads finally to

$$\begin{aligned} GCP(U) &= minG(n;U) = \min\big(F(n) - ne(U_{SHE} - U)\big) \\ &= -\tfrac{1}{4a}\big(b - \mu_{e,SHE} + \text{eU}\big)^2 + c - n_0\mu_{e,SHE} + n_0eU \end{aligned} \quad (4)$$

where

$$n = n_0 - \frac{C_{diff}}{e}(U - U_{PZC})$$

$$GCP(U) = -\frac{C_{diff}}{2}(U - U_{PZC})^2 + n_0eU + F_0 - n_0\mu_{e,SHE}$$

$$F(n) = \frac{e^2}{2C_{diff}}(n - n_0)^2 + \big(\mu_{e,SHE} - eU_{PZC}\big)(n - n_0) + F_0$$

Here G is the grand canonical free energy, which depends on the applied voltage U vs SHE and the number of electrons n, e is the unit electron volt in energy, F is the total free energy as a function of n, and U_{SHE} is the electronic energy at the standard hydrogen electrode (SHE) condition which is –4.44 V. U is defined such that the sign relates directly to the experimental potential, i.e. U = 0.4 V corresponds to 0.4 V vs SHE. For $G(n; U)$ to be used as a *thermodynamic* potential, the number of electrons in the system must be optimized for each applied voltage. Although $F(n)$ appears to be linear with respect to n, as shown in the top graph of Figure S9, this apparent linearity is largely due to the linear contribution of the free energy of electrons. Linearly correcting for the free energies of electrons by plotting $F(n) - nU_{SHE}$ as shown in the bottom plot of Figure S9 reveals that $F(n)$ is quadratic with respect to n.

To obtain the coefficients a, b, and c specific of the structures (all initial, transition, and final states) mentioned in this thesis, we obtained the optimized geometries using VASP at charges that span the potential of interest, then used jDFTx with CANDLE solvation to obtain the free energy and potential (V vs SHE) of the optimized geometry. shows the fitting for $F(n) - nU_{SHE}$ vs $n - n_0$ for the initial states, transition states, and final states for the reactions MoS_2 + $ClCH_3$ on S7 (a low-S sulfur), and on S10 (a high-S sulfur). The initial states and final states for MoS_2 reactions involving one or more sulfurs on the surface were also fitted using this method.

II. Figures

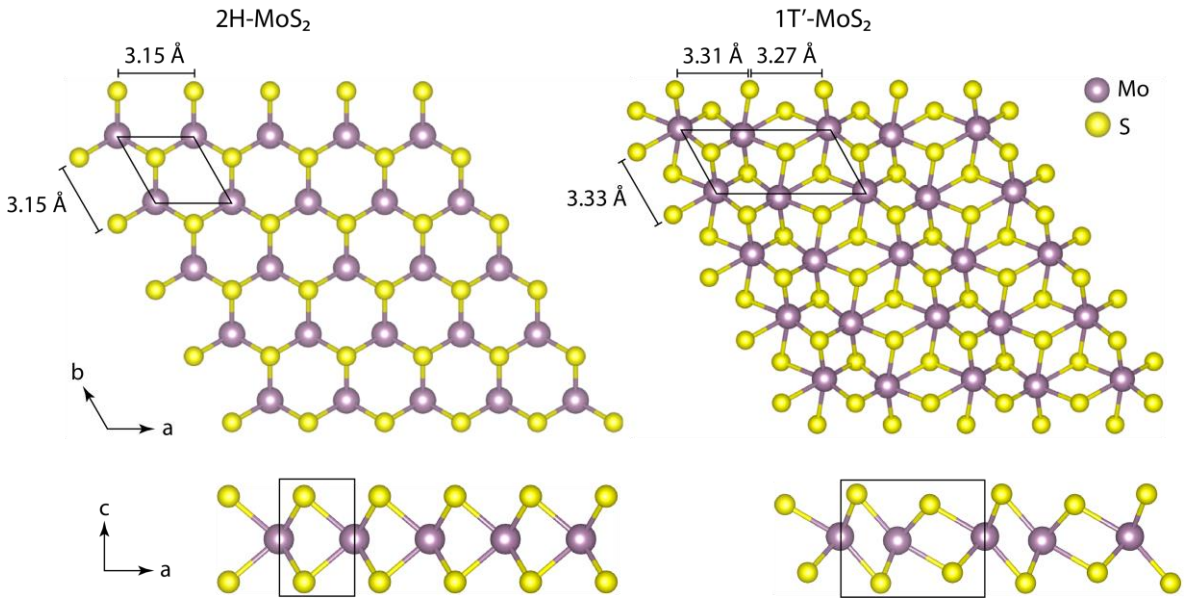

Figure S1. Structure of one layer of 2H-MoS_2 and 1T′-MoS_2 from left to right, viewing top-down along the c-axis and sideways along the b-axis from top to bottom. Boxes outline the unit cells for each structure. Structures were optimized using the results from previously reported work,[6] and labeled values in this figure are based on this work.

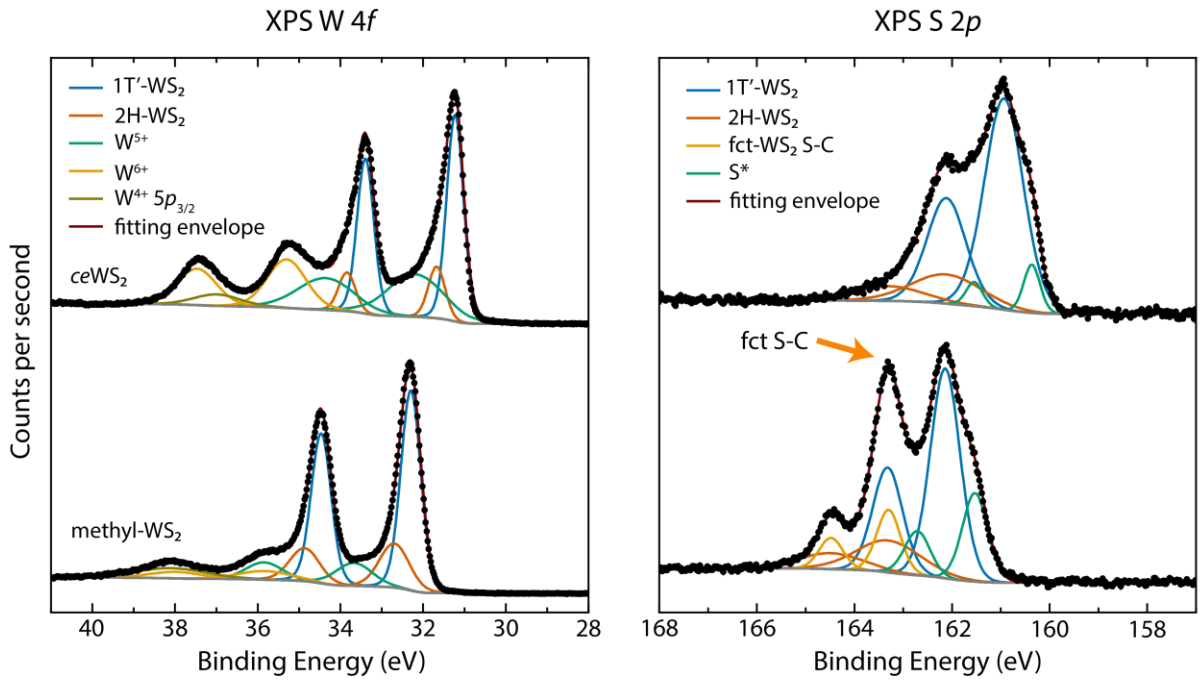

Figure S2. X-ray photoelectron spectra (XPS) of W 4*f* and S 2*p* regions for *ce*WS_2 and methyl-WS_2 synthesized with iodomethane and no reductant. Black dots are the raw data points and lines fit the peaks according to different species. For pure W-containing compounds, W $5p_{3/2}$ separates well from W 4*f*. However, for samples in which W has several chemical states, the W $5p_{3/2}$ signal from lower chemical states overlaps with W $4f_{5/2}$ peak from higher chemical states,[2] which we also observe here.

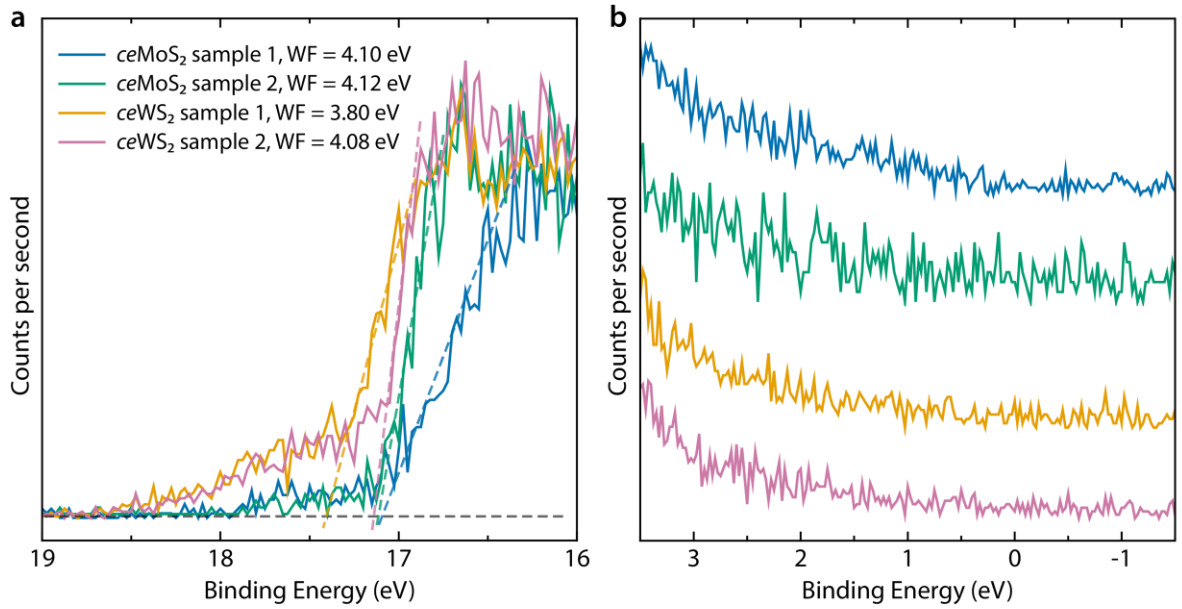

Figure S3. Ultraviolet photoelectron spectra (UPS) of chemically exfoliated MoS_2 and WS_2 samples prepared and transferred under inert atmosphere. (a) The high binding energy cutoff and linear fits used to obtain the work function of dropcast nanosheets. (b) Valence-band regime for the sample samples, showing a band gap near zero, consistent with reported calculations.[6-7]

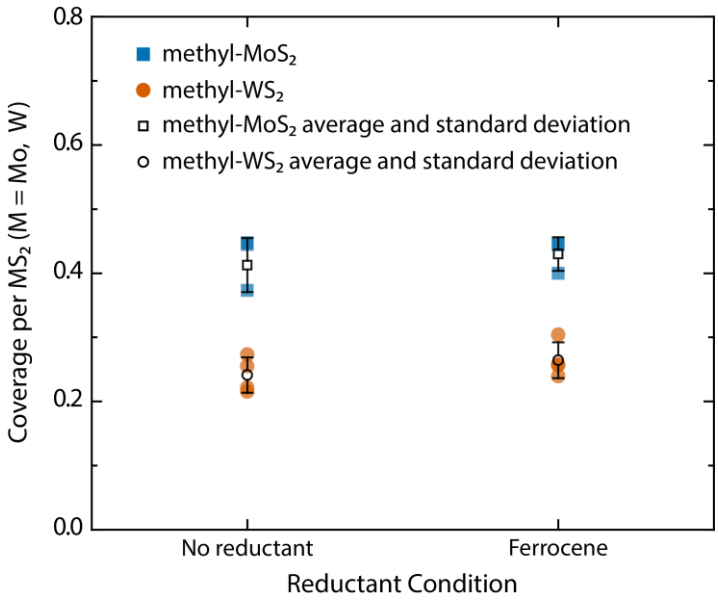

Figure S4. Methyl coverage per MS_2 (M = Mo, W) after reacting with iodomethane either with no reductant added or in the presence of ferrocene, as determined by fitting XPS spectra. Individual points represent a single experiment and hollow symbols indicate the average with standard deviation as error bars. No substantial differences can be observed between these two conditions for neither *ce*MoS_2 nor *ce*WS_2.

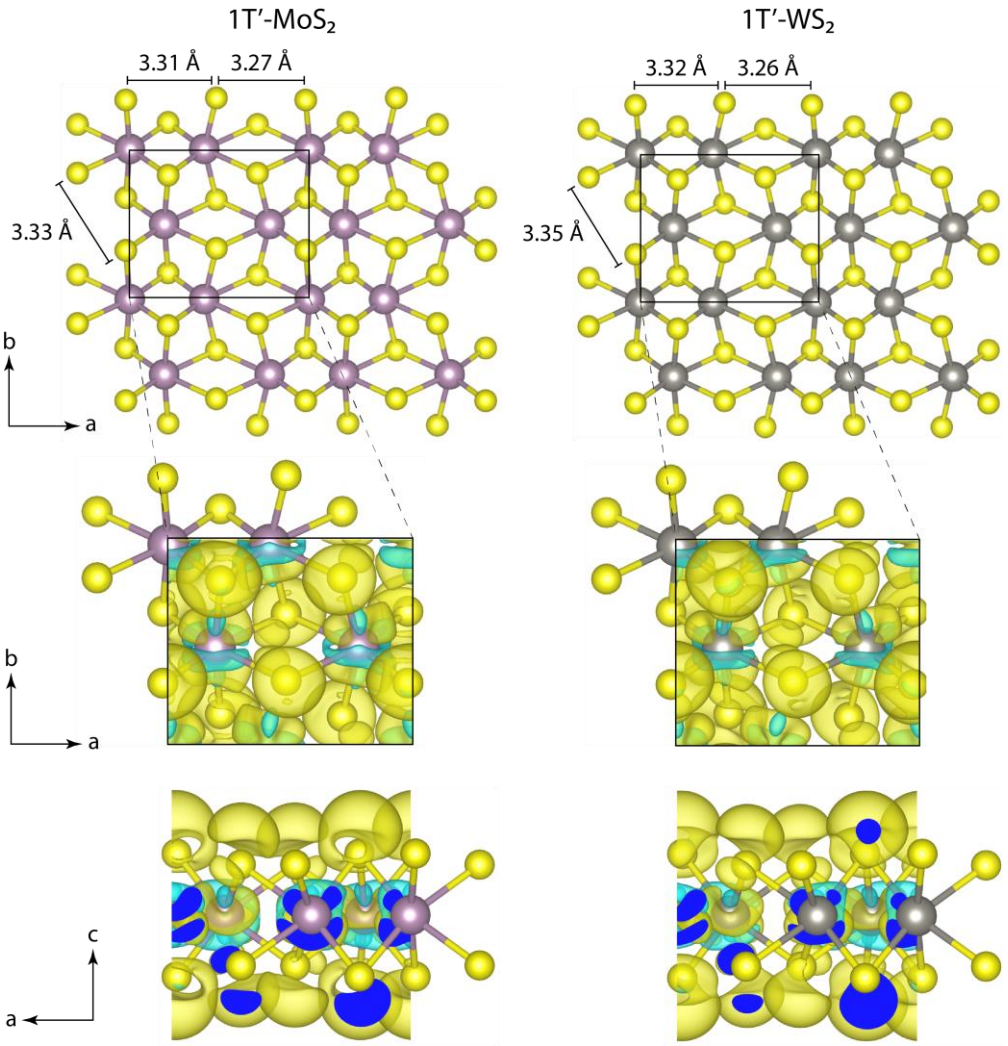

Figure S5. Charge density plot of 1T′-MoS_2 and 1T′-WS_2 using density functional theory (DFT) calculations after optimizing the structures. Charge density was calculated for neutral 1T′-MoS_2 and 1T′-WS_2, and with a -1 charge for both cases, to simulate a net charge of 0.25 per MS_2 (M = Mo, W). The neutral charge density plot was subtracted from the –1 charge density plot for both cases to obtain the charge density difference whose isosurface is shown above. Both structures show similar distribution of the excess negative charge.

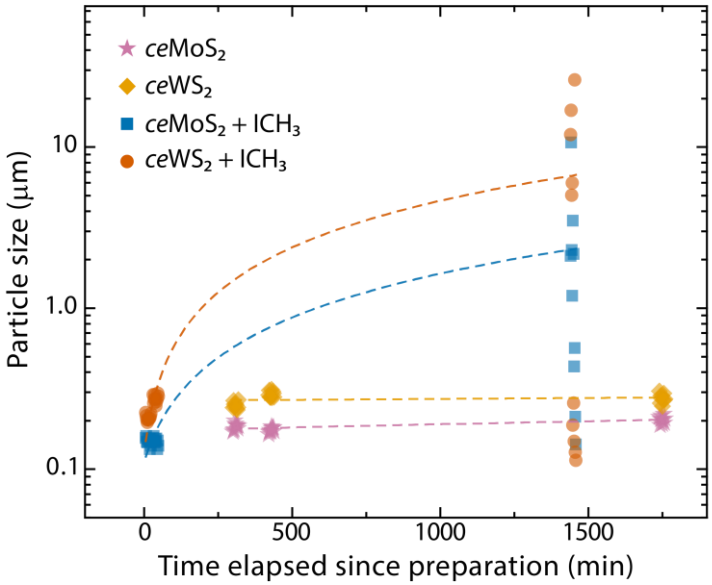

Figure S6. Particle sizes of *ce*MoS_2, *ce*WS_2, *ce*MoS_2 with iodomethane, and *ce*WS_2 with iodomethane as a function of time after sample preparation plotted on a log10 scale for the y-axis. Lines of best fit are generated from least squares linear regression. Each point is an individual measurement, with each cluster containing 10 data points. Opacity of data points is set to 60% to visualize the distribution of overlapping points. The accuracy of particle size measurements decreases above 1 µm, although points above 1 µm indicate the substantial variation and increase in particle size after methyl functionalization that can be attributed to increased aggregation.

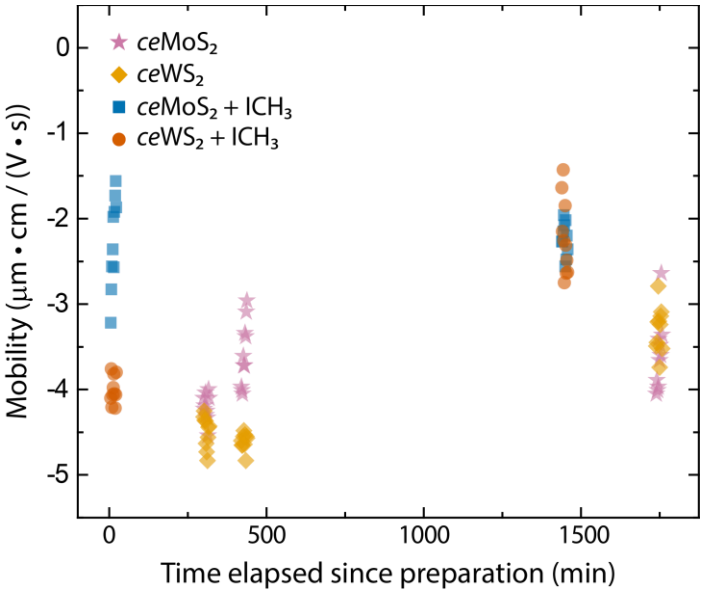

Figure S7. Mobility measurements of particles in suspensions of *ce*MoS_2, *ce*WS_2, *ce*MoS_2 with iodomethane, and *ce*WS_2 with iodomethane, as a function of time since sample preparation using dynamic light scattering. Each point is an individual measurement, with clusters containing 10 data points. Opacity is set to 60% to show distribution of overlapping points. Values plotted here were used to obtain the zeta potentials plotted in Figure 4 using the Smoluchowski model.

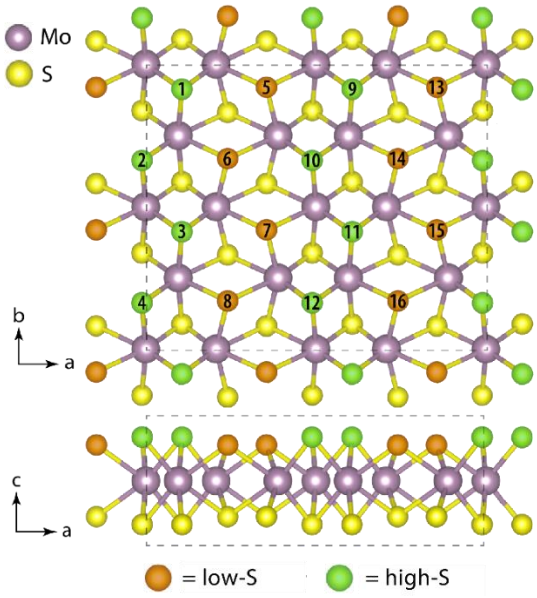

Figure S8. Top-down and side view of the rectangular unit cell of the minimized 1T′-MoS_2 supercell, color-coded to show the two types of sulfur in the unit cell: low-S and high-S, with low-S having a longer average Mo–S distance and high-S having a shorter average Mo–S distance and protruding further out-of-plane compared to the low-S.

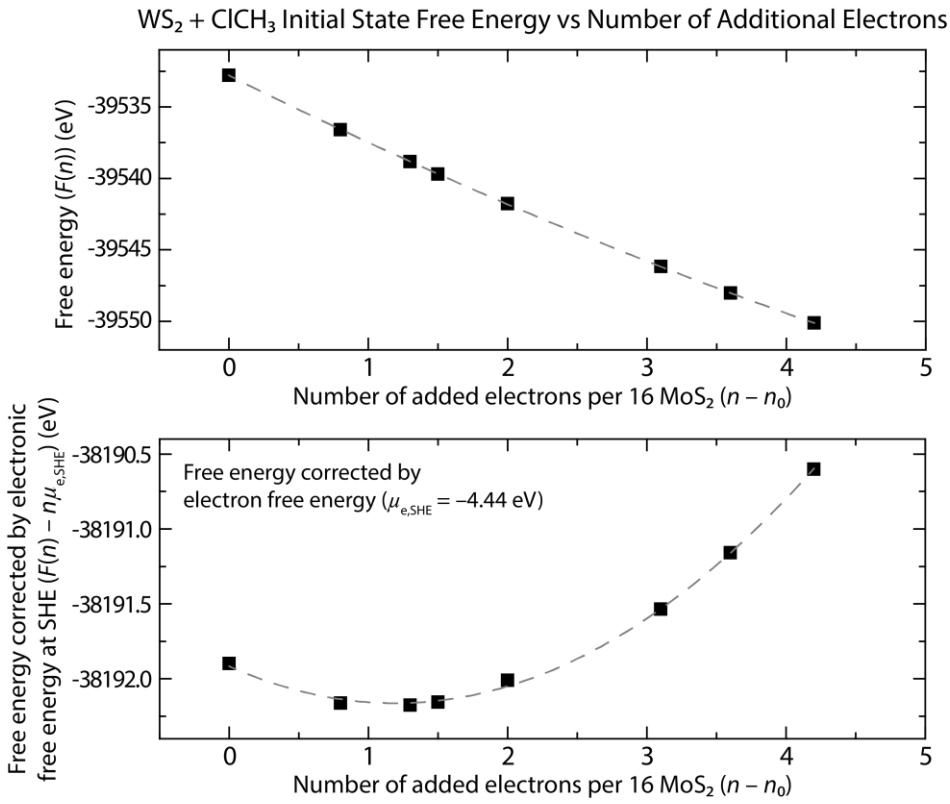

Figure S9. Free energy as a function of the number of electrons relative to the excess charge ($n - n_0$) for the initial state of the WS_2 + $ClCH_3$ reaction on S7, before (top) and after (bottom) correcting for the free energy contribution of electrons. The points are energies calculated using DFT and dashed curves are quadratic fits vs the number of excess electrons ($n - n_0$). The quadratic nature of the free energy dependence on the number of electrons *n* is more apparent once corrected for the free energy contribution of electrons (bottom).

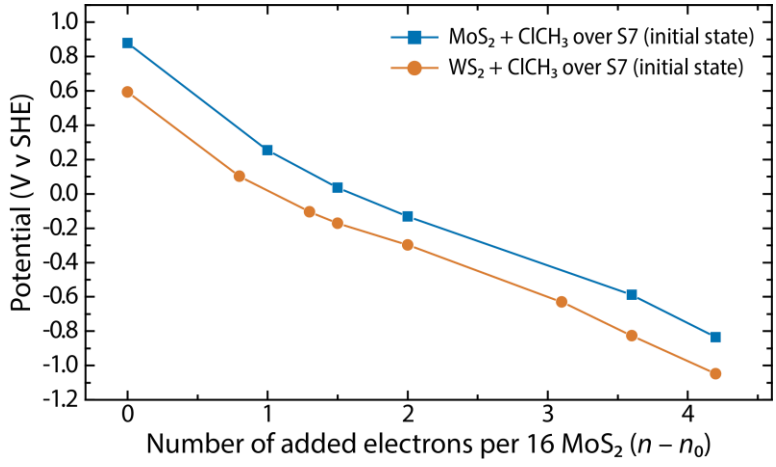

Figure S10. DFT-calculated electrochemical potential in V vs SHE of the initial state structure for the reaction between MS_2 (M = Mo, W) and $ClCH_3$ on S7 as a function of the number of additional electrons in the unit cell.

III. Tables

Table S1. The standard reduction potential for each redox couple, the effective reduction potential assuming 50:1 ratio of reductant to oxidant, and the potential on an absolute energy scale using $E(Fc^{+/0})$ = 0.4 V vs SHE (standard hydrogen electrode) and E_{vac} = –4.44 V vs SHE (see supplementary section I.3).

Reductant (A^-)	Standard Reduction Potential for (A/A^-) vs $E(Fc^{+/0})$ (V)	Effective Reduction Potential, 50:1 reductant to oxidant vs $E(Fc^{+/0})$ (V)	Potential vs E_{vac} (V)
ferrocene, Cp_2Fe	0	–0.10	4.74
nickelocene, Cp_2Ni	–0.42	–0.52	4.32
octamethylnickelocene, Me_8Cp_2Ni	–0.95	–1.05	3.79
cobaltocene, Cp_2Co	–1.16	–1.26	3.58
decamethylcobaltocene, $Me_{10}Cp_2Co$	–1.77	–1.87	2.97

Table S2. Differences between the free energy obtained from interpolation of the quadratic fit of free energy vs number of electrons (example in Figure S9) and the free energy from the DFT calculation on which the fitting is based, at constant potential. For each point used to interpolate the initial, transition, and final states, their free energy and electrochemical potential were calculated using DFT and compared to the free energy value generated by the quadratic fit given the same potential to produce the values in this table. Each reaction is denoted by either MoS_2 or WS_2, and the sulfur methylated by chloromethane ($ClCH_3$), either S7 (low-S) or S10 (high-S).

Charge ($n - n_0$)	Error in free energy (difference between calculated and interpolated GCP free energy) (eV)											
	Initial States				*Transition States*				*Final States*			
	MoS_2 S7	WS_2 S7	MoS_2 S10	WS_2 S10	MoS_2 S7	WS_2 S7	MoS_2 S10	WS_2 S10	MoS_2 S7	WS_2 S7	MoS_2 S10	WS_2 S10
0	0.073	0.064	0.078	–	0.13	–	0.17	–	0.27	–	0.24	–
0.5	–	–	–	7.3e–3	–	–	–	0.059	–	–	–	0.040
0.8	–	–0.024	–	–	–	0.020	–	–	–	0.023	–	–
1	–0.031	–	–0.032	–8.7e–3	–0.064	–	–0.057	–0.024	–0.081	–	–0.071	–0.036
1.3	–	–8.2e–3	–	–	–	–6.6e–3	–	–	–	0.015	–	–
1.5	–1.8e–3	–4.1e–3	1.4e–4	–7.3e–3	–0.030	–4.9e–3	–0.017	–0.022	–0.091	6.2e–5	–0.076	–0.027
2	0.022	0.040	0.022	0.032	0.062	0.021	0.047	0.023	–0.038	1.6e–3	–0.056	0.017
3	–	–	–	–0.018	–	–	–	0.012	–	–	–	0.039
3.1	–	–2.7e–4	–	–	–	–8.1e–3	–	–	–	–7.5e–3	–	–
3.6	0.037	–4.2e–4	0.032	–	0.050	–4.3e–3	0.048	–	0.073	1.4e–3	0.076	–
4.2	–1.2e–4	–4.0e–3	–9.4e–3	0.011	–0.010	6.9e–3	–8.9e–3	–5.8e–3	0.099	2.4e–3	0.089	–4.6e–3
6	–	–	–	–	–	–	–	–	–0.042	–	–0.035	–

Table S3. Particle size measurements of *ce*MoS_2, *ce*WS_2, *ce*MoS_2 with iodomethane, and *ce*WS_2 with iodomethane as a function of time after sample preparation and before the first measurement. Averages and standard deviations are based on 10 measurements, each of which is plotted in Figure S6.

Time elapsed since preparation until first measurement (minutes)	Particle Size (μm) (average ± standard deviation)			
	***ce*MoS_2**	***ce*WS_2**	***ce*MoS_2 + ICH_3**	***ce*WS_2 + ICH_3**
5	–	–	0.149 ± 0.008	0.209 ± 0.009
30	–	–	0.160 ± 0.007	0.272 ± 0.016
300 (5 hours)	0.184 ± 0.009	0.249 ± 0.012	–	–
420 (7 hours)	0.175 ± 0.006	0.291 ± 0.013	–	–
1440 (24 hours)	–	–	2.33 ± 3.14	6.68 ± 8.98
1740 (29 hours)	0.203 ± 0.010	0.276 ± 0.018	–	–

Table S4. Mobility measurements of *ce*MoS_2, *ce*WS_2, *ce*MoS_2 with iodomethane, and *ce*WS_2 with iodomethane as a function of time after sample preparation and before the first measurement. Averages and standard deviations are based on 10 measurements, each of which is plotted in Figure S7.

Time elapsed since preparation until first measurement (minutes)	Particle Size (μm) (average ± standard deviation)			
	***ce*MoS_2**	***ce*WS_2**	***ce*MoS_2 + ICH_3**	***ce*WS_2 + ICH_3**
5	–	–	–2.26 ± 0.53	–4.01 ± 0.16
30	–	–	–2.60 ± 0.20	–3.88 ± 0.16
300 (5 hours)	–4.21 ± 0.16	–4.49 ± 0.19	–	–
420 (7 hours)	–3.59 ± 0.38	–4.61 ± 0.10	–	–
1440 (24 hours)	–	–	–2.24 ± 0.19	–2.22 ± 0.45
1740 (29 hours)	–3.61 ± 0.42	–3.29 ± 0.27	–	–

IV. References

(1) Baltrusaitis, J.; Mendoza-Sanchez, B.; Fernandez, V.; Veenstra, R.; Dukstiene, N.; Roberts, A.; Fairley, N., Generalized Molybdenum Oxide Surface Chemical State XPS Determination via Informed Amorphous Sample Model. *Appl. Surf. Sci.* **2015,** *326*, 151-161.

(2) Qiu, L.; Xu, G., Peak Overlaps and Corresponding Solutions in the X-ray Photoelectron Spectroscopic Study of Hydrodesulfurization Catalysts. *Appl. Surf. Sci.* **2010,** *256*, 3413-3417.

(3) Grimm, R. L.; Bierman, M. J.; O'Leary, L. E.; Strandwitz, N. C.; Brunschwig, B. S.; Lewis, N. S., Comparison of the Photoelectrochemical Behavior of H-Terminated and Methyl-Terminated Si(111) Surfaces in Contact with a Series of One-Electron, Outer-Sphere Redox Couples in CH_3CN. *J. Phys. Chem. C* **2012,** *116*, 23569-23576.

(4) Noviandri, I.; Brown, K. N.; Fleming, D. S.; Gulyas, P. T.; Lay, P. A.; Masters, A. F.; Phillips, L., The Decamethylferrocenium/Decamethylferrocene Redox Couple: A Superior Redox Standard to the Ferrocenium/Ferrocene Redox Couple for Studying Solvent Effects on the Thermodynamics of Electron Transfer. *J. Phys. Chem. B* **1999,** *103*, 6713-6722.

(5) Huang, Y.; Nielsen, R. J.; Goddard, W. A., Reaction Mechanism for the Hydrogen Evolution Reaction on the Basal Plane Sulfur Vacancy Site of MoS_2 Using Grand Canonical Potential Kinetics. *J. Am. Chem. Soc.* **2018,** *140*, 16773-16782.

(6) Chou, S. S.; Sai, N.; Lu, P.; Coker, E. N.; Liu, S.; Artyushkova, K.; Luk, T. S.; Kaehr, B.; Brinker, C. J., Understanding Catalysis in a Multiphasic Two-dimensional Transition Metal Dichalcogenide. *Nat. Commun.* **2015,** *6*, 8311.

(7) Fan, X.-L.; Yang, Y.; Xiao, P.; Lau, W.-M., Site-specific Catalytic Activity in Exfoliated MoS_2 Single-layer Polytypes for Hydrogen Evolution: Basal Plane and Edges. *J. Mater. Chem. A* **2014,** *2*, 20545-20551.